PHYSICAL REVIEW FLUIDS **5**, 114601 (2020)

Cooperative drag reduction in turbulent flows using polymer additives and superhydrophobic walls

Anoop Rajappan and Gareth H. McKinley[*]
Hatsopoulos Microfluids Laboratory, Department of Mechanical Engineering,
Massachusetts Institute of Technology, Cambridge, Massachusetts 02139, USA

(Received 24 April 2020; accepted 1 September 2020; published 6 November 2020)

The addition of soluble long chain polymers to a Newtonian fluid, and the incorporation of aerophilic textures on submerged solid boundaries, have both been successfully employed as independent, stand-alone methods for drag reduction in turbulent aqueous flows. In this paper, we explore the possibility of combining the two strategies additively to obtain enhanced levels of frictional drag reduction in wall-bounded turbulence. By means of skin friction measurements in fully turbulent Taylor-Couette flow, we show that dissolved polymer chains act in concert with superhydrophobic walls to yield a net reduction in turbulent drag that is up to 50% greater than that obtainable from either method employed independently. Cooperative drag reduction measurements are presented for various combinations involving one of two common water-soluble polymers (either polyacrylamide or polyethylene oxide) paired with one of two prototype drag-reducing superhydrophobic surfaces—either a regular pattern of streamwise microgrooves or a scalable random superhydrophobic texture possessing hierarchical multiscale roughness. The surface activity of polyethylene oxide is observed to adversely influence the wall slip on the randomly textured surface, leading to significant diminution in the overall drag reduction efficacy of this polymer-surface combination. In cases where such interfacial effects are absent, an additive friction law in Prandtl-von Kármán coordinates is proposed that yields fairly accurate predictions of the combined drag reduction performance anticipated from a given polymer-surface pair, each possessing known individual drag-reducing characteristics.

DOI: 10.1103/PhysRevFluids.5.114601

I. INTRODUCTION

Turbulent aqueous flows constitute an essential feature of numerous real-life flow systems [1,2]: common examples include the flow of water in pipes, sewers, district heating networks and fire hoses, the transportation of crude oil via long-distance pipelines, the drag-inducing boundary layer over the hulls of ships and submarines, and even the flow of blood in the large arteries of the human body. Given its ubiquitous importance in wide-ranging engineering and commercial applications, the mitigation of frictional losses in turbulent flows is of great engineering and practical interest, offering the potential for significant economic and environmental benefits. For example, turbulent skin friction on the hull accounts for about 50% of the total drag on ships and about 60% of the drag on submarines under routine operating conditions [3]; an estimated 60% of the propulsive power of a typical ship is expended solely in overcoming this boundary layer drag. [4]. Techniques to mitigate skin friction drag, even moderately, thus have the potential to yield considerable savings in

---

[*] gareth@mit.edu

©2020 American Physical Society

fuel consumption and operating costs, along with attendant improvements in propulsive efficiency and reductions in exhaust emissions into the atmosphere.

The addition of soluble, long chain polymers has long been known to be an effective strategy for reducing frictional drag in turbulent flows [5–8]. Even at dilute concentrations amounting to only a few tens of parts per million by weight, dissolved polymer chains can interact with and alter the dynamics of near-wall turbulent flow structures, suppressing momentum transport to the wall and yielding concomitant reductions in frictional shear stress of 20–40% [5,8]. The phenomenon of turbulent drag reduction by polymeric solutes has been extensively investigated in numerous experimental [5–7] and computational studies [8–10] spanning the seven decades since its discovery, and a wide range of synthetic, as well as naturally occurring, high polymers have been successfully employed as drag reducing agents in various turbulent flow configurations [11,12].

More recently, following rapid advances in surface fabrication technologies over the last two decades, superhydrophobic texturing of the wetted flow boundaries has also emerged as an alternative method of drag reduction in wall-bounded aqueous flows [13–17]. Drag-reducing superhydrophobic surfaces incorporate chemically hydrophobic roughness features which enable them to trap and retain a thin layer of air—called the *plastron*—that remains pinned to the texture asperities, even when the surface is fully submerged underwater [13,14,17]. This plastron layer, in turn, shields the liquid from direct contact with the underlying solid over large areal fractions of the flow boundary, as confirmed through direct confocal imaging of the air-water interface [18,19]. Even as the usual no-slip condition continues to hold in wetted regions of solid-liquid contact, the liquid-air interface atop the plastron serves as a nearly shear-free boundary over which the flow slips with minimal friction. The effect of this composite boundary condition on the outer flow is often modeled by an equivalent homogeneous slip velocity V_s at the wall, given by the Navier slip condition $V_s = b\,\tau_w/\eta$; here η is the dynamic viscosity of the liquid, τ_w is the average shear stress at the wall, and b represents an average "effective" slip length characterizing the superhydrophobic texture [14]. Despite early successes in laminar drag reduction—with the first positive experimental results dating as far back as 1996 [20]—progress towards the use of superhydrophobic surfaces in turbulent flows has been relatively slow, due in part to challenges in fabricating robust textures capable of sustaining an intact plastron layer even under the intense pressure fluctuations typically encountered in turbulence [17,21]. Several such surfaces have, nevertheless, been developed in recent years, and turbulent drag reductions of up to 50% on periodically micropatterned surfaces, and up to 30% on scalable randomly textured surfaces, have been reported in the current literature [17,22,23].

As a result of these developments, we now have available two distinct routes to realizing practicable drag reduction in turbulent flows: (i) dissolved polymer chains, which suppress momentum transport across the turbulent boundary layer, and (ii) plastron-bearing superhydrophobic surfaces which, in effect, induce a slip velocity locally at the wall. Despite sustained research interest in both techniques as stand-alone methods for drag mitigation in turbulent flows, the question of employing them concurrently to enhance the overall drag reduction effect has largely been neglected in the extant literature. In an accompanying report, we demonstrate that a cooperative deployment of these two drag reduction mechanisms is indeed possible: polymers and superhydrophobic surfaces are shown to combine additively to yield friction reductions larger than that obtainable from either method operating alone [24]. This was accomplished through measurements of skin friction in fully turbulent Taylor-Couette (TC) flow, employing a superhydrophobic inner wall composed of a periodic array of streamwise grooves, in conjunction with a nonionic and surface-inactive drag-reducing polymer (polyacrylamide) added to the liquid inside the flow gap. In the present paper, we extend the work reported therein to explore additional combinations of polymers and superhydrophobic textures, and to address practical concerns pertinent to real-life applications. A description of experimental techniques, including the use of a bespoke Taylor-Couette apparatus for turbulent wall-friction measurements, is first provided in Sec. II. In Sec. III, we present experimental results demonstrating the combined drag reduction effect using a readily scalable superhydrophobic texture possessing random surface roughness. Subsequently, we also investigate the adverse influence of interfacial effects that accompany the use of a common drag-reducing polymer additive—namely, polyethylene oxide or PEO—which is known to adsorb at the air-water interface, thereby influencing the effective slip boundary condition that prevails over the trapped plastron layer atop the superhydrophobic wall.

II. EXPERIMENTAL METHODS

A. Skin friction measurements in turbulent Taylor-Couette flow

To assess the drag reduction performance of polymer additives and superhydrophobic surfaces, both individually and in parallel, we performed experimental measurements of frictional drag on the inner cylindrical wall of a bespoke Taylor-Couette apparatus, operated at speeds sufficiently high to generate featureless, fully turbulent shear flow inside the cell gap. Figure 1(a) shows a schematic sectional view of the apparatus and its key components. The rotating inner cylinder (the "rotor") is machined from aluminum 6061-T6 alloy, and has radius $R_i = 38.1\,\text{mm}$ and axial length $L = 76.2\,\text{mm}$; its exterior cylindrical surface was either polished smooth for no-slip flow measurements or suitably processed to generate the requisite superhydrophobic texture for use in drag reduction tests (as described in Sec. II B). The coaxial stationary outer cylinder (the "stator") enclosing the rotor is made of transparent cast acrylic and has radius $R_o = 50.8\,\text{mm}$, thereby creating an annular flow gap of width $d = R_o - R_i = 12.7\,\text{mm}$ in which the working fluid (water or dilute polymer solution) is contained; this yields a radius ratio of $R_i/R_o = 0.75$ and a geometric aspect ratio of $L/d = 6.0$ for our particular TC geometry. The rotor is coupled to and driven by a commercial controlled-stress rotational rheometer (AR-G2, TA Instruments), enabling precise measurements of the angular speed Ω, and the steady-state frictional torque $\mathcal{T}$ exerted by the working fluid on the cylindrical rotor wall. The rotor is designed to have a hollow interior recess which remains air-filled during experiments, thereby providing a shear-free interface at the bottom that eliminates extraneous torque which would otherwise arise from fluid friction acting on the lower face. The bespoke TC apparatus has previously been extensively tested in the course of our prior experimental work on drag-reducing superhydrophobic textures [23] and biopolymer solutions [25], and further details of its construction and flow characteristics may be found in these earlier reports.

We define the Reynolds number $\text{Re} = \rho V d/\eta$ for the TC flow in the annular gap based on the gap width d, the speed $V = R_i\Omega$ of the rotating inner wall, and the density ρ and viscosity η of the working fluid. In the current flow configuration wherein the inner cylinder rotates and the outer one remains stationary, the primary Couette flow is unstable to radial perturbations above a critical rate of rotation, and transitions through a series of secondary vortex flow regimes with increasing angular speed Ω of the rotor (or, equivalently, the Reynolds number Re) [26]. At large Reynolds numbers, these vortex structures become turbulent and eventually disappear completely, and featureless, fully turbulent, wall-driven shear flow is attained in the annular gap [26]. This final transition to featureless turbulent flow in our bespoke TC apparatus occurs at a critical Reynolds number $\text{Re}_c = 11\,000$; this was determined by analyzing the scaling of the baseline frictional torque $\mathcal{T}$ with the Reynolds number Re, measured using a smooth no-slip rotor in deionized water [27]. Subsequent tests employing drag-reducing polymers and superhydrophobic surfaces were performed at Reynolds numbers $15\,000 \leqslant \text{Re} \leqslant 52\,000$, ensuring that the flow inside the TC gap lies well inside the turbulent flow regime.

All flow measurements were conducted at room temperature, measured to be $(21.0 \pm 0.5)\,^\circ\text{C}$ during tests involving the randomly textured superhydrophobic surface, and $(23.0 \pm 0.5)\,^\circ\text{C}$ in all other cases. A typical flow test involved varying the angular velocity Ω of the rotor in discrete steps, and recording the mean steady-state frictional torque $\mathcal{T}$ at constant rotor speed. The average wall shear stress $\tau_w = \mathcal{T}/2\pi R_i^2 L$, and the friction velocity $u_\tau = \sqrt{\tau_w/\rho}$ in the near-wall layer, were then calculated from the experimental torque versus speed data. Finally, the shear Reynolds number was computed based on the gap width as $\text{Re}_\tau = \rho u_\tau d/\eta$. The reference viscosity η here was set equal to either the viscosity of water $\eta_w(T)$ or, in tests involving drag-reducing polymers, the

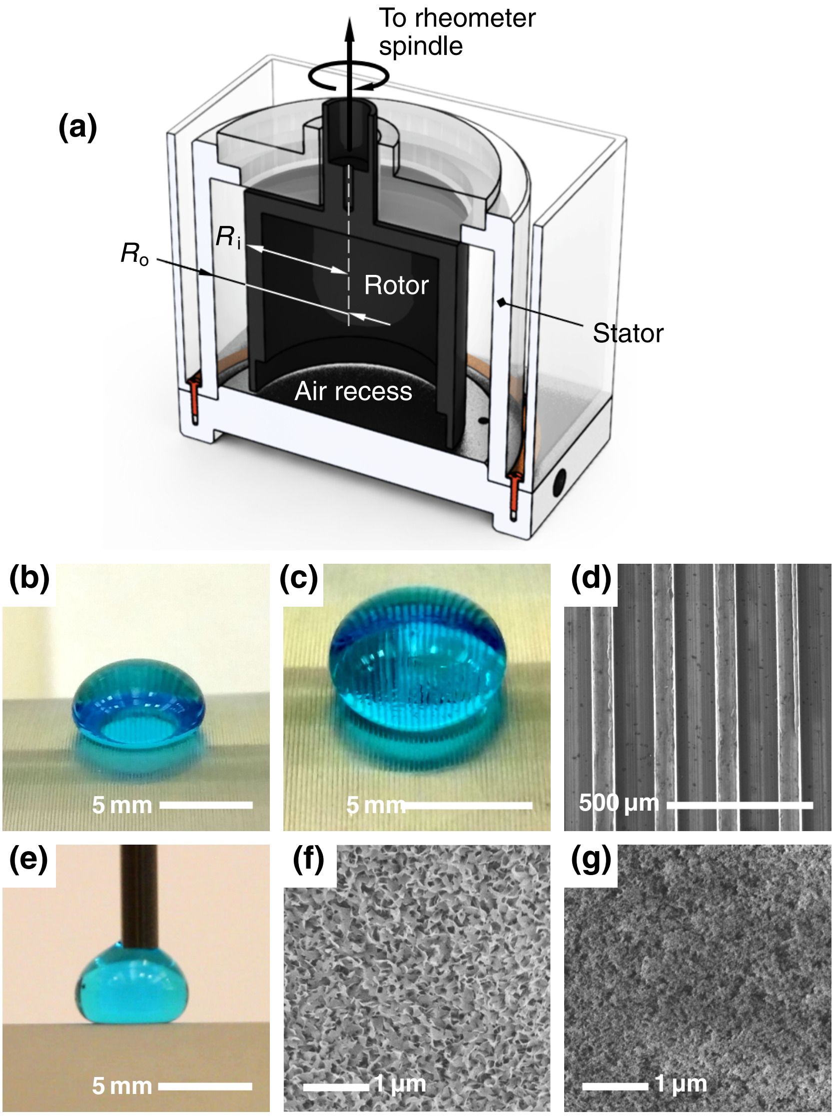

FIG. 1. (a) Schematic sectional view of the bespoke TC apparatus used for turbulent drag measurements. The entire fixture is mounted on a commercial rotational rheometer, which is not shown. (b) A water drop, dyed blue, placed on the surface of the superhydrophobic grooved rotor. A reflective plastron is visible at the circular base of the drop. (c) A closer image of the basal surface of the drop in panel (b). The individual plastrons filling the groove troughs appear magnified due to optical refraction through the spherical drop cap. (d) Scanning electron micrograph of the grooved surface shown in panels (b) and (c). The grooves are aligned circumferentially along the exterior rotor surface. (e) A drop of water, colored blue, deposited on the superhydrophobic random texture. (f) Scanning electron micrograph of the random texture before hydrophobization with Glaco solution. The characteristic crossed leaflet nanostructure of boehmite is clearly visible. (g) The random texture in panel (f) after treatment with Glaco solution, showing the underlying boehmite layer completely covered by hydrophobic silica nanoparticles.

zero shear viscosity $\eta_0(T)$ of the dilute polymer solution, at the corresponding test temperature T. Prior to tests employing a superhydrophobic rotor wall, the working fluid was allowed to aerate freely inside a ventilated container for several hours to reach air saturation at ambient temperature, so as to prevent undue depletion of the plastron layer by diffusion of gas into the liquid phase. Furthermore, the experimental procedure was carefully designed to mitigate effects of flow-induced polymer degradation: freshly prepared solutions were used in each experiment and then discarded after the test, the total duration of each test (about 6 min) was kept well below the typical time scale for chain scission [which was determined by regression of degradation data to the well-known Brostow expression to be characterized by a rate constant of $r \approx (12\,\text{min})^{-1}$ [25]], and the rotor speeds were traversed from low to high so as to minimize undue effects of degradation at the later steps. For each flow curve, multiple replicate experiments were performed and the data sets were averaged before subsequent analysis; the number of replicates used in each test is indicated in the respective figure legends.

B. Fabrication of drag-reducing superhydrophobic surfaces

We performed flow measurements on two different plastron-bearing superhydrophobic surfaces: a regularly patterned array of streamwise grooves, and a scalable texture composed of hierarchical random roughness at multiple length scales. The processes involved in their fabrication is briefly described in this section.

1. Superhydrophobic grooved surface

To fabricate the superhydrophobic grooved surface (subsequently denoted S_G), regularly spaced rectangular grooves were machined into the outer wall of the aluminum rotor using a lathe; the grooves were aligned parallel to the circumferential (streamwise) direction, and spaced evenly along the rotor axis spanning the full height of its exterior cylindrical surface. The machined grooves were hydrophobized by dip coating in a dilute ($\approx$0.1%) solution of a water-repellent fluoropolymer resin (Teflon AF 2400, Chemours), and subsequently baked at elevated temperature on a hot plate following manufacturer guidelines (175 °C for 10 min to evaporate the solvent, followed by 5 min at 245 °C above the glass transition temperature of the resin, and finally at 330 °C for 15 min to enhance adhesion). The dip-coating and baking steps were repeated at least five times to yield a mechanically durable hydrophobic layer firmly adhering to the underlying aluminum substrate. Inspection of the final texture under a scanning electron microscope (SEM) revealed a well-formed groove profile coated uniformly by a conformal layer of hydrophobic resin, with no appreciable levels of secondary nanoscale roughness. Figure 1(b) shows a sessile water drop deposited on the cylindrical rotor surface; a closer view of the drop base can be seen in Fig. 1(c), wherein the individual plastrons bridging the groove crests are clearly discernible. A representative micrograph of the grooved surface is shown in Fig. 2(d). Similar SEM images, obtained at multiple spots on the rotor surface, were used to determine an average spatial periodicity of $l = 204$ µm and a gas fraction of $\phi = 0.66$ for the groove pattern (i.e., corresponding to a wetted solid fraction of $1 - \phi = 0.34$).

2. Superhydrophobic random texture

The superhydrophobic random texture (hereafter denoted S_R) used in our experiments was prepared identically to the 80-grit sandblasted, etched, and boehmitized aluminum surface reported in our earlier work [23] (and designated "SEB-80" in that study). The random texture was created by sequentially sandblasting the rotor surface with 80-grit media (average particle size of 165 µm), etching in 12 M (37% by volume) hydrochloric acid for 25 s, and finally boehmitizing in boiling deionized water for 30 min. The surface was then treated with a commercial water-repellent coating (Glaco Mirror Coat Zero, SOFT99, Japan) composed of 30–50 nm hydrophobic silica particles dispersed in 2-propanol. The textured rotor was dip coated in the Glaco solution, dried in ambient air for 10%, and subsequently baked for 30 min at 200° on a hot plate; the coating

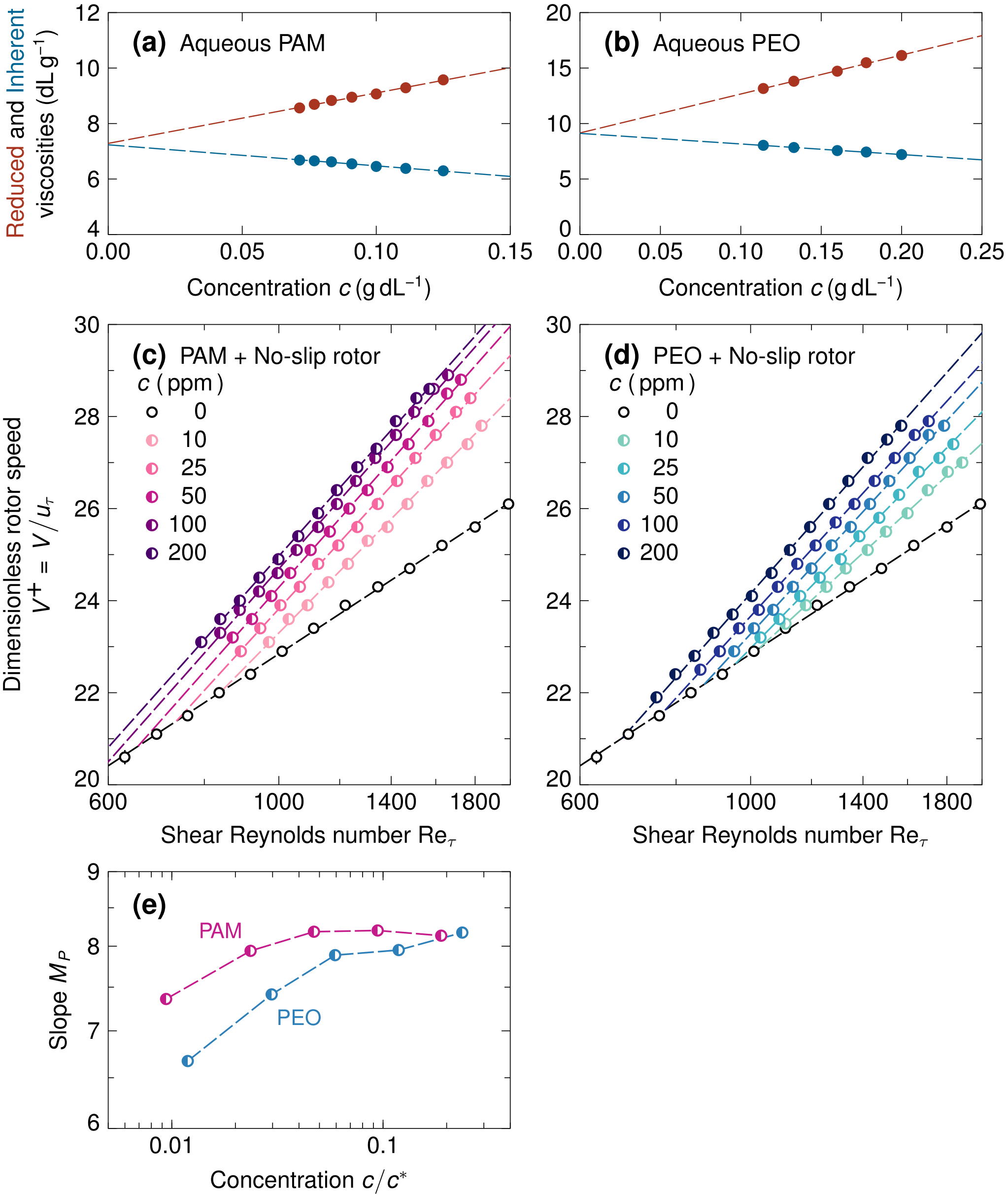

FIG. 2. (a), (b) Huggins-Kramer plots for (a) aqueous PAM and (b) aqueous PEO solutions, used in the experimental determination of the intrinsic viscosity [η]. (c), (d) Experimental friction curves for the smooth no-slip rotor in aqueous solutions of (c) PAM and (d) PEO of various concentrations, showing turbulent drag reduction induced by the dissolved polymer chains. The black hollow circles in both panels denote the baseline friction data for the smooth rotor in deionized water. Data are averaged over two replicates. (e) The slope M_P of the polymeric friction curve as a function of the normalized concentration c/c^*, obtained by linear least-squares regression of Eq. (2) to the experimental data in panels (c) and (d).

and baking steps were repeated thrice to ensure a robust coating with uniform areal coverage. As reported in our previous study, this process yields a superhydrophobic surface possessing multiple tiers of hierarchical roughness [see Figs. 1(e)–1(g)], with advancing and receding contact angles of $\theta_A = (152 \pm 1)^\circ$ and $\theta_R = (148 \pm 1)^\circ$, respectively [23]. Figures 1(f) and 1(g) show scanning electron micrographs of the superhydrophobic random texture before and after treatment with the Glaco solution; the porous boehmite layer helps support and retain the hydrophobic silica on the aluminum substrate, and is seen to be completely overspread by nanoparticles after three rounds of dip coating and baking.

C. Preparation of aqueous drag-reducing polymer solutions

As model drag-reducing polymers, we employed dilute solutions of aqueous polyacrylamide (PAM) and polyethylene oxide (PEO), each composed of flexible, linear, nonionic chains with large molar masses $\approx 10^6\,\mathrm{g\,mol^{-1}}$. Both polymers were procured in powder form (Sigma-Aldrich Inc) and used as is without further purification. First, a 0.4% stock solution of each polymer was prepared by gently dispersing the requisite quantity of powder in deionized water, and allowing it to hydrate and dissolve gradually on a laboratory bench roller over several days to ensure uniform laminar mixing. Solutions of various concentrations c, for use in flow tests, were subsequently prepared by diluting this stock solution with an appropriate volume of deionized water.

As a direct characterization of the effective macromolecular properties of our drag-reducing solutions, we determined the intrinsic viscosity $[\eta]$ for each of the two polymers in water, adopting the conventional procedure of extrapolating both the reduced viscosity $\eta_{\mathrm{red}} = (\eta_0 - \eta_w)/\eta_w c$ and the inherent viscosity $\eta_{\mathrm{inh}} = \ln(\eta_0/\eta_w)/c$ concurrently to zero concentration [28]. The zero shear rate viscosity η_0 of the solution at different concentrations was measured using a glass-capillary dilution viscometer of the Ubbelöhde type (size 0B, Cannon Instrument Company), which was kept suspended in a water bath at controlled temperature. In Figs. 2(a) and 2(b), the experimental viscometry data for each polymer are presented in the form of a Huggins-Kramer plot, in the regime where η_{red} and η_{inh} show a linear dependence on the concentration c of the dissolved polymer. When extended to zero concentration, the two lines meet at a common intercept that represents the intrinsic viscosity $[\eta]$ of the specific polymer [28]; this procedure yielded intrinsic viscosities of $[\eta]_{\mathrm{PAM}} = 7.26\,\mathrm{dL\,g^{-1}}$ and $[\eta]_{\mathrm{PEO}} = 9.13\,\mathrm{dL\,g^{-1}}$ for PAM and PEO chains in water, respectively. The intrinsic viscosity $[\eta]$ may, in turn, be related to the viscosity-averaged molar mass M_v of the dissolved chains, by means of the empirical Mark-Houwink-Sakurada equation $[\eta] = K M_v^a$ [29]. Utilizing values of the constants K and a available in the literature [30,31], we inferred a viscosity-averaged molar mass of approximately $M_{v,\mathrm{PAM}} \approx 2.54 \times 10^6\,\mathrm{g\,mol^{-1}}$ for our PAM sample, and $M_{v,\mathrm{PEO}} \approx 1.72 \times 10^6\,\mathrm{g\,mol^{-1}}$ for PEO.

Furthermore, the critical overlap concentration c^* for flexible chains in good solvents may be estimated [29] from their intrinsic viscosity as $c^* = 0.77/[\eta]$, resulting in an overlap concentration of $c^*_{\mathrm{PAM}} = 1.1\,\mathrm{g\,L^{-1}}$ for aqueous PAM, and $c^*_{\mathrm{PEO}} = 0.84\,\mathrm{g\,L^{-1}}$ for aqueous PEO. The solutions used in our flow tests were considerably more dilute with concentrations c in the range of 10–200 ppm, corresponding to normalized concentrations of $0.009 \leqslant c/c^* \leqslant 0.24$. Viscometric data for the various dilute polymer solutions used in our drag reduction experiments are listed in Table I.

III. RESULTS AND DISCUSSION

A. Drag reduction measurements

Below, we report experimental drag measurements in turbulent Taylor-Couette flow of water as well as dilute PAM and PEO solutions, with and without a superhydrophobic texture present on the rotor wall. For ease of discussion, the results have been organized into five sections on the basis of the working fluid inside the gap (water or polymer solution) and the flow boundary condition (no-slip superhydrophobic grooves or superhydrophobic random texture) at the rotor surface.

TABLE I. Concentration c and relative viscosity $\eta_r = \eta_0/\eta_w$ of dilute PAM and PEO solutions used in experimental drag measurements. The relative viscosities reported are averaged values derived from capillary viscometry of each test solution.

Polymer	Concentration c (ppm)	Concentration c/c^*	Relative viscosity $\eta_r = \eta_0/\eta_w$
Polyacrylamide ($[\eta]_{\mathrm{PAM}} = 7.26\,\mathrm{dL\,g^{-1}}$)	10	0.0094	1.01
	25	0.024	1.02
	50	0.047	1.04
	100	0.094	1.08
	200	0.19	1.15
Polyethylene oxide ($[\eta]_{\mathrm{PEO}} = 9.13\,\mathrm{dL\,g^{-1}}$)	50	0.059	1.05
	200	0.24	1.19

1. *Water plus no-slip rotor*

For fully turbulent Taylor-Couette flow of a Newtonian fluid with a rotating inner cylinder, Panton [32] used matched asymptotic expansions for the azimuthal angular momentum in the flow gap to derive a logarithmic friction law of the form

$$V_N^+ = M \ln \mathrm{Re}_\tau + N, \tag{1}$$

where $V^+ = V/u_\tau$ is the rotor wall speed in inner units, the subscript N denotes Newtonian flow, and M and N are constants that depend on the radius ratio R_i/R_o of the TC geometry. We note that the quantity V^+ may also be expressed as $V^+ = (2/C_f)^{1/2}$, where the nondimensional skin friction coefficient C_f is given by $C_f = 2\tau_w/\rho V^2$. In Figs. 2(c) and 2(d), experimental friction data are presented in Prandtl–von Kármán coordinates, wherein V^+ is plotted as a function of the shear Reynolds number Re_τ on semilogarithmic axes. The friction data for the smooth no-slip rotor in deionized water in the fully turbulent regime [hollow black circles in Figs. 2(c) and 2(d)] show good conformance to the functional form predicted by Eq. (1), and a linear least-squares regression of Eq. (1) to this baseline data was used to obtain the constants $M = 4.76$ and $N = -10.0$ for our bespoke TC apparatus.

2. *Polymer solution plus no-slip rotor*

To characterize the drag reduction efficacy of the aqueous PAM and PEO solutions, we performed friction measurements on the smooth, no-slip rotor, employing dilute solutions of different concentrations of each polymer as the working fluid in the cell gap. The resulting data are shown in Figs. 2(c) and 2(d), respectively, for dilute PAM and PEO solutions of different concentrations c. Analogous to the case of turbulent drag reduction in pipe flows [6], the experimental friction data in polymer solutions are well described by straight lines on the Prandtl–von Kármán plot of the form

$$V_P^+ = M_P \ln \mathrm{Re}_\tau + N_P, \tag{2}$$

where the subscript P denotes polymer drag reduction, and the constants M_P and N_P, obtained from linear least-squares fits to the data, now depend also on the polymer species used and its concentration c in solution. The drag-reducing effect of the dissolved polymer chains is evidenced by the larger slope $M_P > M$ of the polymeric friction curves, and its upward divergence from the Newtonian baseline in the turbulent regime. This becomes more apparent if we consider the skin friction coefficient $C_f = 2\tau_w/\rho V^2$, which may equivalently be expressed as $C_f = 2/(V^+)^2$; a larger value of V^+ therefore implies a smaller value of the friction coefficient C_f and, by extension, a reduced wall shear stress τ_w at the same imposed speed V of the rotor wall. As expected, the drag reduction effect becomes larger with increasing Reynolds number, and at greater concentrations of

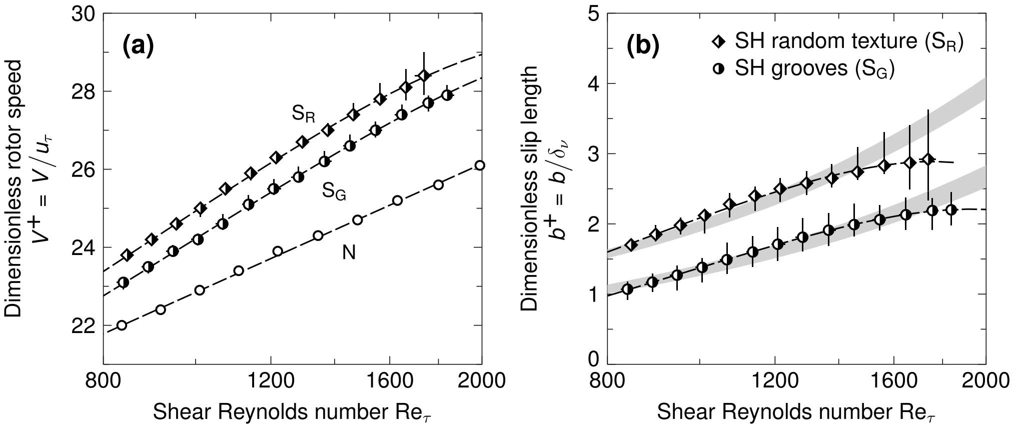

FIG. 3. (a) Experimental friction curves for the grooved rotor (S_G) and the randomly textured rotor (S_R) in air-saturated deionized water, showing drag reduction induced by wall slip. The baseline data for the no-slip rotor (N) are also included for comparison. (b) The nondimensional slip length b^+ for the two superhydrophobic rotors, derived from the data in panel (a), shown as a function of the shear Reynolds number Re_τ. The dashed curves represent least-squares quadratic polynomial fits to the data. The two gray bands denote, respectively, the expected linear variation of b^+ for a constant (dimensional) slip length of $b = (17 \pm 1)$ μm for the grooved rotor S_G, and $b = (25 \pm 1)$ μm for the randomly textured rotor S_R. Error bars in both panels show the full range of observations across multiple replicate tests (ten replicates for S_G, and six for S_R).

the dissolved polymer [6]. Figure 2(e) shows the variation of the slope M_P with the normalized polymer concentration c/c^* for aqueous PAM and PEO solutions, as determined empirically from linear fits of Eq. (2) to the data in Figs. 2(c) and 2(d).

3. Water plus superhydrophobic rotor

Figure 3(a) shows the experimental friction curves for both the grooved and randomly textured superhydrophobic rotors, as measured in deionized, air-saturated water. The skin friction law for the turbulent TC flow of a Newtonian fluid with an effective slip boundary condition at the inner wall was derived by Srinivasan *et al.* [18], and is given by

$$V_S^+ = M \ln \mathrm{Re}_\tau + N + b^+, \tag{3}$$

where the subscript S denotes a superhydrophobic rotor wall, $b^+ = b/\delta_\nu$ is the effective slip length b expressed in wall units ($\delta_\nu = \eta/\rho u_\tau = d/\mathrm{Re}_\tau$ being the viscous length scale of the turbulent boundary layer), and the constants M and N are identical to those determined for the baseline no-slip case, Eq. (1). Drag reduction arising from the effective wall slip at the plastron-bearing texture on the rotor surface is again evident as an upward shift in each of the superhydrophobic friction curves relative to the no-slip baseline. In Fig. 3(b), we plot the nondimensional slip length b^+, computed from the experimental friction data using Eq. (3), as a function of the shear Reynolds number Re_τ. We note that for a constant effective slip length b at the wall the dimensionless slip length $b^+ = b/\delta_\nu = b\,\mathrm{Re}_\tau/d$ increases linearly with Re_τ. As seen in Fig. 3(b), the effective wall slip b^+ for both superhydrophobic surfaces increases initially with the shear Reynolds number, but subsequently saturates at high rotor speeds, owing to a decrease in the physical slip length b caused by the progressive flow-induced collapse of the plastron layer over the texture. To capture this gradual variation at high Reynolds numbers, the experimentally measured slip lengths on the two superhydrophobic rotors were individually fit to simple quadratic functions of the form $b^+ = A + B\,\mathrm{Re}_\tau + C\,\mathrm{Re}_\tau^2$, denoted by the dashed curves in Figs. 3(a) and 3(b); this was done to facilitate smooth interpolation of the slip length at intermediate values of the shear Reynolds numbers Re_τ in later analyses.

The effective slip lengths over an alternating pattern of no-slip and shear-free stripes at the wall were derived analytically by Philip [33] in the limit of viscous creeping flows, and are given by the expressions $b_\parallel = (l/\pi)\ln\sec(\pi\phi/2)$ in the direction parallel to the stripe pattern, and $b_\perp = b_\parallel/2$ in the direction perpendicular to it. By contrast, in turbulent flows, the effective slip length derives from a complex interplay of both the streamwise and spanwise slip lengths on the texture; in essence, spanwise slip serves to strengthen near-wall vortices and enhances momentum transport, thus partly offsetting the drag reduction induced by streamwise slip through forward displacement of the mean velocity profile [34]. The effective slip length thus depends nontrivially on the local tensorial slip pattern at the wall and the viscous length scale of the inner flow, and a quantitative prediction for generic surface textures is typically possible only using computational methods. The above complexities notwithstanding, we may obtain a very rough estimate of the anticipated slip length on our grooved texture [35] as $b \approx b_\parallel - b_\perp = (l/2\pi)\ln\sec(\pi\phi/2) = 22\ \mu\mathrm{m}$, which is indeed consistent with the average (dimensional) slip length of $b = 17\ \mu\mathrm{m}$ measured in our experiments over the finite range of Reynolds numbers investigated. For the superhydrophobic random texture, experimental friction data in Fig. 2 yield an average slip length of $b = 25\ \mu\mathrm{m}$, in excellent agreement with the value of $b = 24\ \mu\mathrm{m}$ reported for the identically fabricated SEB-80 texture in our earlier study [23].

4. Polymer solution plus superhydrophobic grooved rotor

Having characterized the drag-reducing efficacy of each of the two polymers and the two superhydrophobic surfaces individually, we next proceed to perform frictional drag measurements combining the two techniques, first employing the superhydrophobic grooved rotor in conjunction with aqueous PAM and PEO solutions; representative data for the case of the grooved rotor in combination with the 50-ppm aqueous PAM solution are shown as curve C_G in Fig. 4(a). The friction curves for the no-slip rotor in 50-ppm PAM solution (curve P) and for the grooved rotor in water (curve S_G)—reproduced from Figs. 2(c) and 3(a) above—are also included for comparison. Over the entire range of Reynolds numbers investigated, the combined drag reduction levels are observed to be larger than that produced by either technique employed independently, confirming that the two mechanisms indeed operate conjointly in an additive fashion, enhancing the overall drag reduction that can be achieved in turbulent flow. From a practical standpoint, the quantity that is often of immediate interest in engineering applications is the net decrease in fluid friction (i.e., the reduction in the wall shear stress in external flows, or the reduction in the pressure drop per unit length in internal flows) that can be obtained in comparison to the flow of the unmodified fluid over no-slip walls under identical conditions of imposed wall speed or flow rate. Accordingly, we define the percentage drag reduction as $\mathcal{D} = (1 - \tau_w/\tau_{w,N}) \times 100\%$, where τ_w is the actual shear stress measured at the rotor wall with either one or both drag reduction mechanisms in operation, and $\tau_{w,N}$ is the baseline shear stress on the no-slip rotor in deionized water at the same rotor speed V (or, equivalently, at the same solvent-based Reynolds number $\mathrm{Re}_s = \rho V d/\eta_w$ defined using the viscosity η_w of pure water). In Fig. 4(b), the data in Fig. 4(a) have been replotted in terms of the percentage drag reduction $\mathcal{D}$ versus the Reynolds number Re_s, and the enhancement in the overall drag reduction arising from combining polymers with a superhydrophobic wall (curve C_G) is again apparent.

In an accompanying paper, we propose a two-layer model for the combined drag reduction effect that leads to an additive friction law in Prandtl-von Kármán coordinates of the form [24]

$$(V_C^+)^\circ = V_P^+ + (V_S^+ - V_N^+) = M_P \ln \mathrm{Re}_\tau + N_P + b^+, \tag{4}$$

where the subscript C denotes the "combined" (or "composite") drag reduction effect, and the superscript $^\circ$ indicates an ideal estimate derived from the additive framework described therein.

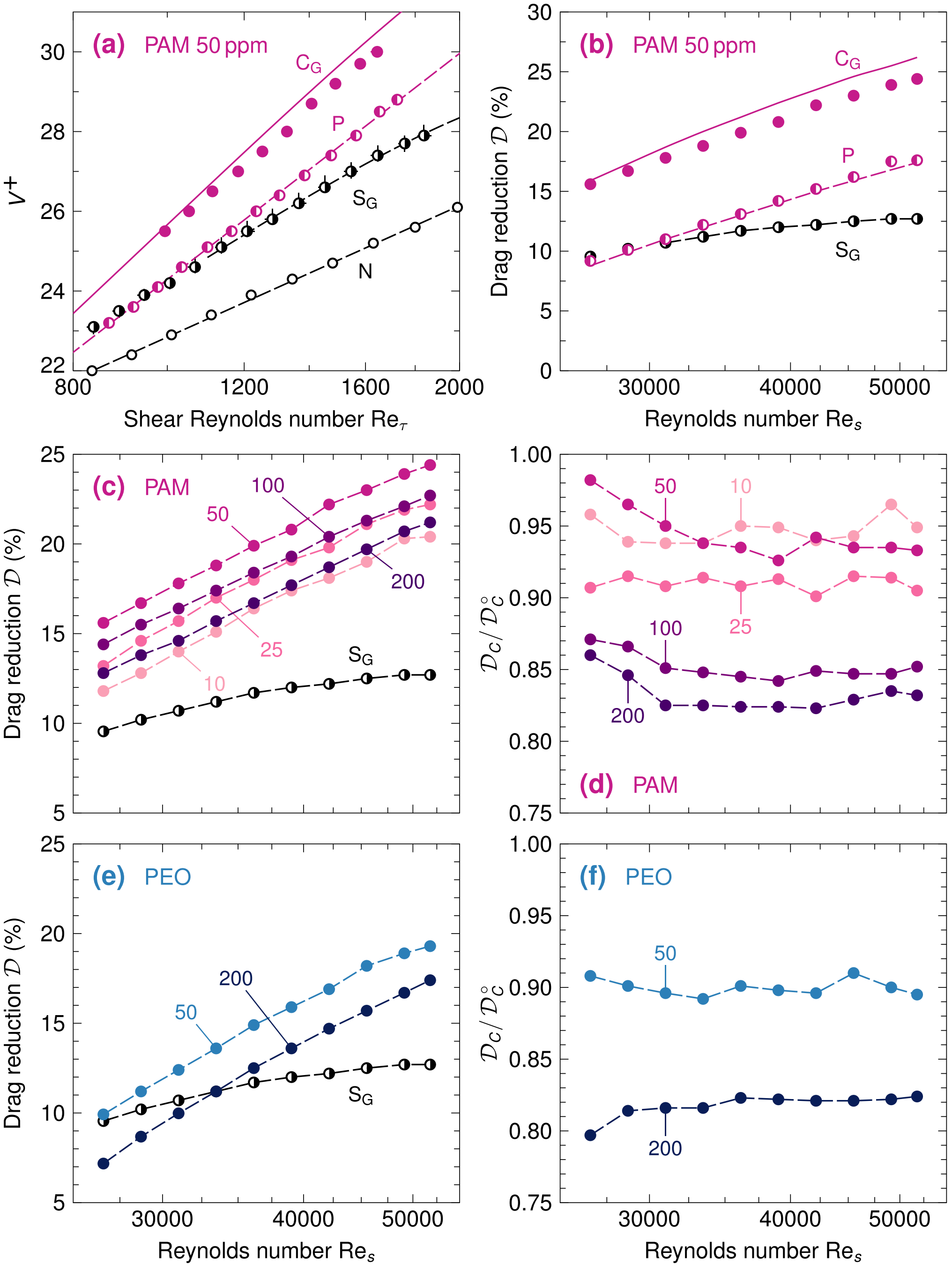

FIG. 4. (a) Combined drag reduction data (labeled C_G) for the superhydrophobic grooved rotor in a 50-ppm solution of aqueous PAM. Also included for comparison are the individual friction curves for the no-slip rotor in water (N) and in 50-ppm aqueous PAM (P), as well as for the superhydrophobic grooved rotor in deionized water (S_G). (b) The percentage drag reduction $\mathcal{D}$ corresponding to the data shown in panel (a). The solid curves in panels (a) and (b), respectively, denote the ideal drag reduction estimates $(V_C^+)^\circ$ and $\mathcal{D}_C^\circ$ predicted by Eqs. (4) and (9). (c) Percentage drag reduction for the grooved rotor in PAM solutions of various concentrations.

Rearranging Eq. (4) into the form

$$(V_C^+)^\circ - V_N^+ = (V_P^+ - V_N^+) + (V_S^+ - V_N^+), \tag{5}$$

we see that this expression simply represents an addition of the velocity increments at a given value of Re_τ from the individual polymeric and superhydrophobic friction curves, to construct the combined friction law in Prandtl–von Kármán coordinates. Obtaining the corresponding estimate for the percentage drag reduction $\mathcal{D}_C^\circ$, at a given Reynolds number Re_s, is less straightforward because of the nonlinear relationship between the wall shear stress (or the shear Reynolds number) and the imposed wall speed (or the solvent-based Reynolds number) represented by Eq. (4). Denoting the value of Re_τ by x, and substituting the relation $V^+ = V/u_\tau = \mathrm{Re}_s/\eta_r\,\mathrm{Re}_\tau$ in Eq. (4), we obtain

$$\mathrm{Re}_s = \eta_r\, x[M_P \ln x + N_P + b^+(x)], \tag{6}$$

which is an implicit nonlinear equation to be solved for $x = \mathrm{Re}_\tau$. With the slip length b^+ approximated by a quadratic polynomial of the form $b^+(x) = A + Bx + Cx^2$ as discussed above (see Sec. III A 3), Eq. (6) does not in general admit a closed-form solution in elementary functions. We therefore employ Halley's iterative method [36]

$$x_{n+1} = x_n - \frac{2f(x_n)f'(x_n)}{2[f'(x_n)]^2 - f(x_n)f''(x_n)} \tag{7}$$

to locate the root $\hat{x}$ of the function $f(x) = \mathrm{Re}_s - \eta_r\, x[M_P \ln x + N_P + b^+(x)]$, from which $(V_C^+)^\circ = \mathrm{Re}_s/\eta_r\,\hat{x}$ can be computed. Similarly, the baseline friction law, Eq. (1), may be inverted to yield

$$V_N^+ = M\, W\!\left(\frac{\mathrm{Re}_s}{M}\, e^{N/M}\right), \tag{8}$$

where $W(z)$ denotes (the principal branch of) the product logarithm function (also known as the Lambert W function). The additive estimate for the percentage drag reduction can then be obtained simply as

$$\mathcal{D}_C^\circ(\mathrm{Re}_s) = \{1 - [V_N^+/(V_C^+)^\circ]^2\} \times 100\%, \tag{9}$$

for a specified value of the wall speed V (or, equivalently, for a specific value of the solvent-based Reynolds number $\mathrm{Re}_s = \rho V d/\eta_w$).

In Figs. 4(a) and 4(b), the solid curves represent the wall friction as predicted by the additive law, Eq. (4), and the corresponding estimate for the percentage drag reduction $\mathcal{D}_C^\circ$ computed using Eq. (9), for the grooved superhydrophobic rotor in 50-ppm PAM solution. While there is good agreement with experimental data, especially at lower Reynolds numbers ($\mathrm{Re}_s \leqslant 30\,000$), the actual drag reduction levels [denoted by the filled circles in Figs. 4(a) and 4(b)] are seen to be consistently smaller than the ideal value predicted by the additive model (represented by the solid line in the above plots). In Fig. 4(c), the percentage drag reduction $\mathcal{D}_C$ measured on the grooved rotor is shown as a function of the Reynolds number Re_s at different concentrations c of aqueous PAM. The percentage drag reduction achieved is observed to initially increase with increasing polymer concentration, attain a maximum, and subsequently fall off at concentrations exceeding 50 ppm. This latter decline at large polymer concentrations can be ascribed to the increasing shear viscosity $\eta_0(c)$ of the polymer solution, which enhances the overall viscous dissipation in the flow and thereby detracts from the drag reduction induced by polymeric suppression of turbulence. Figure 4(d) shows

---

(continued) The individual numbers denote the polymer concentration c in ppm. (d) The ratio $\mathcal{D}_C/\mathcal{D}_C^\circ$ of the actual drag reduction achieved as compared to the ideal estimate, for the data shown in panel (c). (e), (f) Drag reduction data for the grooved rotor in aqueous PEO, analogous to those presented for PAM in panels (c) and (d). Drag reduction data in panels (a)–(d) were averaged over at least three replicates, and those in panels (e) and (f) were averaged over six replicates.

the ratio of the actual drag reduction $\mathcal{D}_C$ to the ideal value $\mathcal{D}_C^\circ$ predicted by Eq. (9), and attests to the predictive utility of our simple empirical model; the actual drag reduction $\mathcal{D}_C$ is within 90% of the model prediction $\mathcal{D}_C^\circ$ for concentrations $c \leqslant 50$ ppm, and is within 80% of the predicted value for concentrations up to 200 ppm. Thus the additive law, in general, yields a good first estimate of the total drag reduction achievable in dilute polymer solutions, but progressively overpredicts the combined effect as the polymer concentration c is increased. Finally, Figs. 4(e) and 4(f) show analogous curves for drag measurements on the superhydrophobic grooved rotor in PEO solutions at two different concentrations; except for the smaller overall drag reduction in comparison to PAM solutions due to a more pronounced viscous effect (arising from the larger value of $[\eta]_{\mathrm{PEO}}$), the results are otherwise seen to be qualitatively similar.

5. Polymer solution plus randomly textured superhydrophobic rotor

Lastly, as a proof of concept demonstration of the combined drag reduction technique using scalable superhydrophobic surfaces, we performed drag measurements on the randomly textured rotor in 50-ppm aqueous solutions of PAM and PEO. The resulting friction curves are plotted in Figs. 5(a) and 5(c) in Prandtl–von Kármán coordinates, and the corresponding percentage drag reduction curves are shown in Figs. 5(b) and 5(d). In aqueous PAM, our experimental results mirror the case of superhydrophobic grooves discussed in Sec. III A 4 above, and the additive law yields an excellent prediction for the combined drag reduction levels actually observed. In stark contrast, the combined drag reduction measured in the aqueous PEO solution falls well short of the ideal drag reduction levels predicted by Eqs. (4) and (9). In fact, as seen in Fig. 5(d), the combined percentage drag reduction at Reynolds numbers $\mathrm{Re}_s \leqslant 40\,000$ is smaller than the purely superhydrophobic drag reduction observed when no PEO is added to the water. The markedly different results obtained for PAM and PEO solutions is intriguing, inasmuch as both polymers are composed of flexible, linear, nonionic chains with comparable macromolecular properties. In the next section, we provide insight into this "anomalous" behavior of poly(ethylene oxide) by considering the preferential adsorption of amphiphobic PEO chains at the plastron interface.

B. Interfacial effects

A number of commonly employed drag-reducing polymers—both synthetic (such as PEO) and bio-sourced (such as xanthan gum)—are known to exhibit surface activity in aqueous solutions [37,38], and at chemical equilibrium exist with a fraction of their dissolved chains preferentially adsorbed at the air-water interface. For example, the (—CH_2–CH_2—) alkyl moiety of the ethylene oxide repeat unit is sufficiently hydrophobic to render PEO chains surface active, and as a result PEO depresses the equilibrium surface tension when added to water [37]. Furthermore, the presence of trace contaminants or chemical impurities, often unavoidable in industrial practice, could suffice to impart significant surfactant activity to solutions of otherwise surface-inactive polymer samples. Even if the diminution in surface tension is insufficient to precipitate an outright collapse of the plastron layer (followed by transition to the fully wetted, drag-increasing Wenzel state [17]), the presence of adsorbed surfactant molecules can nevertheless have a significant impact on the shear-free properties of the air-water interface that we desire to promote on superhydrophobic textures. For instance, Peaudecerf *et al.* [39] have recently shown that even at trace concentrations of surfactants the external flow can generate a surfactant gradient along the plastron layer which, in turn, induces adverse Marangoni stresses that diminish, or even completely eliminate, slip at the wall; the air-water interface in this case essentially behaves like a rigid, no-slip boundary.

To ascertain the possibility of surfactant effects interfering with the slip characteristics of our superhydrophobic rotors, we measured the surface tension of aqueous PAM and PEO solutions over a range of concentrations at 23 ° C using the Wilhelmy plate method. The data are shown in Fig. 6(a); barring experimental uncertainties, the surface tension of water remained unaltered (at $\sigma \approx 72\,\mathrm{mN\,m^{-1}}$) with the addition of PAM, but was reduced to approximately $\sigma \approx 62\,\mathrm{mN\,m^{-1}}$ in

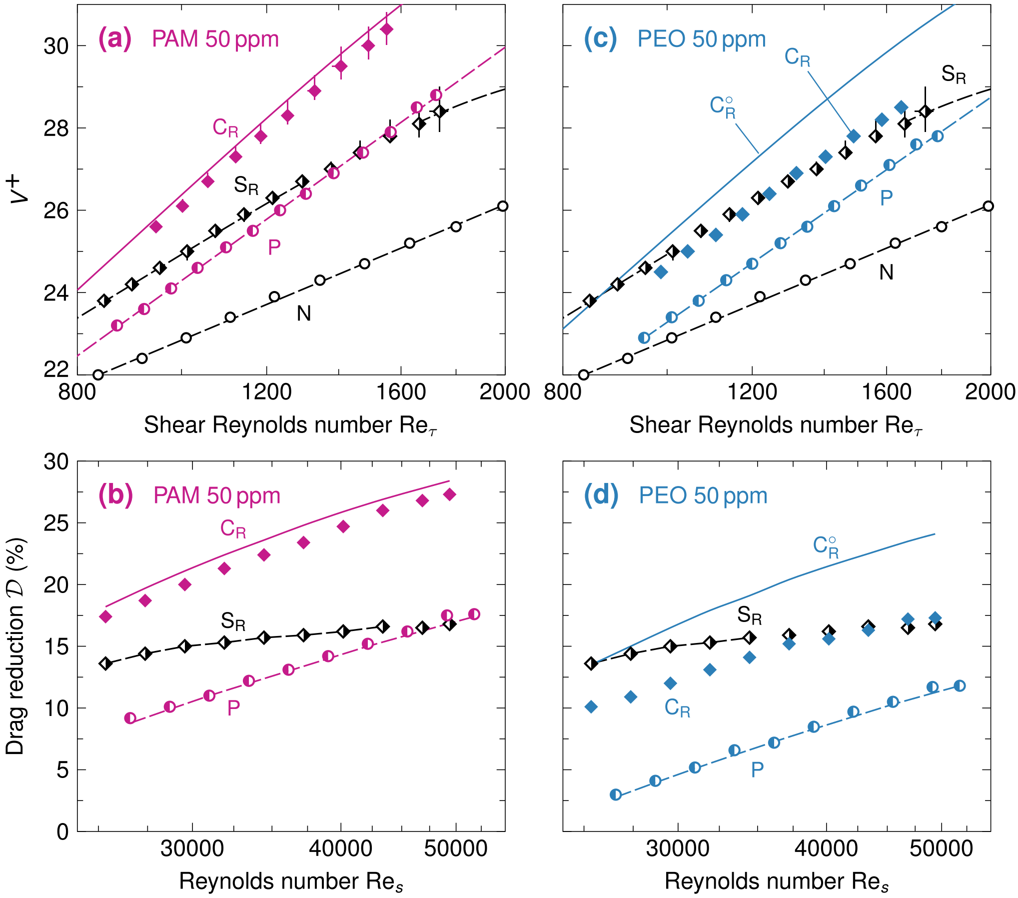

FIG. 5. (a) Combined drag reduction data (labeled C_R) for the randomly textured superhydrophobic rotor in a 50-ppm solution of aqueous PAM. The individual friction curves for the no-slip rotor in water (N) and in 50-ppm aqueous PAM (P), and for the randomly textured rotor in deionized water (S_R), are also included for comparison. (b) The percentage drag reduction $\mathcal{D}$ corresponding to the data shown in panel (a). The solid curves in panels (a) and (b), respectively, denote the ideal additive estimates $(V_C^+)^\circ$ and $\mathcal{D}_C^\circ$ predicted by Eqs. (4) and (9). (c), (d) Drag reduction curves for the randomly textured rotor in 50-ppm aqueous PEO, analogous to the data for PAM shown in panels (a) and (b). In the case of PEO, the actual drag reduction observed in experiments (labeled C_R) falls considerably short of the ideal estimate denoted by the solid curves (separately labeled C_R° for clarity). Drag reduction data in panels (a) and (b) were averaged over six replicates, and those in panels (c) and (d) were averaged over eight replicates.

the presence of dissolved PEO at concentrations used in flow tests. These measurements are in excellent concordance with the data reported in prior literature [37,40], and confirm the non-negligible adsorption of PEO chains at the air-water interface, as well as the absence of such interfacial effects in aqueous PAM solutions.

To simulate the influence of dissolved PEO on the extent of wall slip that can be achieved—in isolation from its drag-reducing properties—we performed experimental friction measurements on the two superhydrophobic rotors in a 0.5% solution of 2-butanol in water; butanol was chosen on account of its excellent miscibility with water, and its low volatility at room temperature. As seen in Fig. 6(b), adding 0.5% by volume of butanol lowers the surface tension of water to approximately $\sigma \approx 63\,\mathrm{mN\,m^{-1}}$, which is very close to the surface tension of the PEO solutions

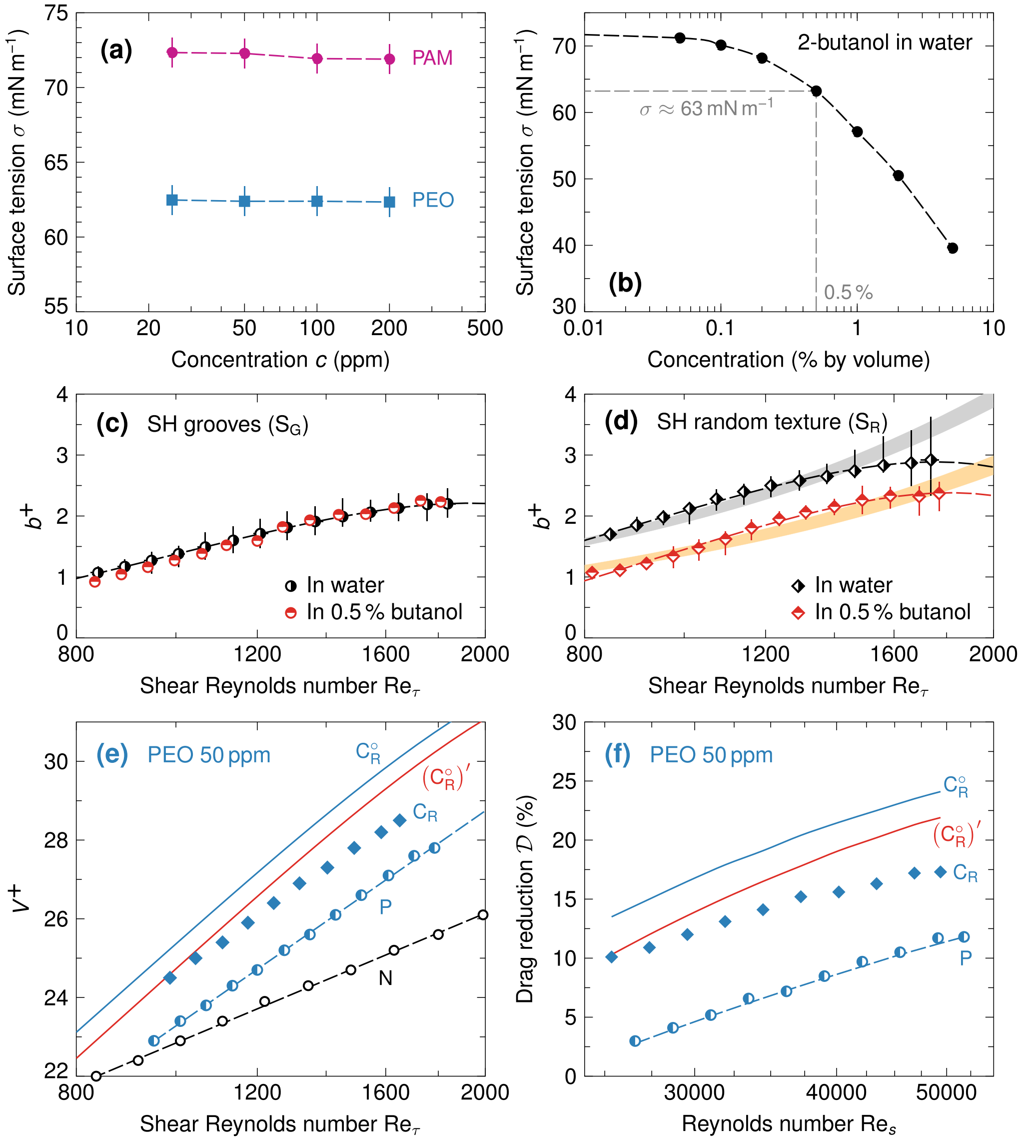

FIG. 6. (a) Surface tension σ of aqueous PAM and PEO solutions as a function of the polymer concentration c. The surface tension of water is unaltered by the addition of PAM, and that of the PEO solution is largely independent of c within the range of concentrations employed in flow tests. (b) Surface tension of a binary solution of 2-butanol in water, as a function of the percentage volume of butanol. (c, d) Experimentally determined slip length b^+ on the grooved rotor (c) and the randomly textured rotor (d) in a 0.5% solution of butanol in water. The original slip length curves for the two rotors as measured in pure water—and shown in Fig. 3(b)—are also included for comparison. In panel (d), the gray and orange bands denote the expected variation of b^+ for constant slip lengths of $b = (25 \pm 1)\ \mu\text{m}$ and $(18 \pm 1)\ \mu\text{m}$, for the randomly textured rotor in water and in the butanol solution, respectively. (e, f) Ideal drag reduction estimates for the randomly textured superhydrophobic rotor in 50-ppm aqueous PEO, recomputed based on the diminished slip length determined from panel (d). The revised predictions are denoted by the orange solid curves labeled $(C_{\rm R}^{\circ})'$; all other curves are identical to those in Figs. 5(c) and 5(d).

used in our flow tests. Figures 6(c) and 6(d) show the experimentally determined slip length b^+ for the two superhydrophobic surfaces immersed in the butanol-water system; the original slip length curves for each surface as measured in deionized water, shown in Fig. 3(b), are also included for comparison. As evident from the plot, the effective slip on the grooved rotor is largely unaffected by the presence of adsorbed [41] butanol at the interface, which is consistent with the observations of Peaudecerf *et al.* [39]. The lack of transverse flow barriers across the continuous circumferential pattern on the grooved rotor precludes the shear-induced development of surfactant gradients and attendant Marangoni stresses (which require the presence of stagnation lines against which surfactant molecules can accumulate). In contrast, the average slip length on the superhydrophobic random texture is appreciably diminished (from $b \approx 25$ to 18 μm) in the butanol solution. This may either be a consequence of adverse Marangoni stresses, arising from surfactant gradients that form adjacent to flow-obstructing texture asperities, or may also be due to the lowering and further impalement of the air-water interface into the random texture, caused by the reduction in the surface tension of the liquid phase [42].

In Figs. 6(e) and 6(f), we replot the friction data for the superhydrophobic random texture in 50-ppm aqueous PEO [shown earlier in Figs. 5(c) and 5(d)], but now with our additive estimate [orange solid curves labeled $(C_{\mathrm{R}}^{\circ})'$] rederived based on the reduced slip length actually measured in the butanol-water solution [as reported in Fig. 6(d) and denoted by orange markers]. While there is now improved agreement between the predicted values and experimental data, it is also apparent that this simple correction in the extent of wall slip attained is still inadequate to completely account for the drag reduction deficit observed on the random texture in the presence of PEO molecules. Numerical investigations of wall-bounded turbulence that take into account both surfactant kinetics as well as the dynamics of the partially rigidified air-water interface established atop the random texture may be required to fully elucidate the complex interactions of near-wall turbulence, interfacial gradients, and wall slip in combined drag reduction when employing surface active polymers such as PEO.

IV. CONCLUSION

To summarize, we have shown that dilute concentrations of polymer additives can be deployed jointly with superhydrophobic surface treatments to augment the overall drag reduction that can be achieved in wall-bounded turbulent shear flows. The cooperative drag reduction effect was studied by pairing one of two flexible drag-reducing polymer additives—PAM and PEO—in conjunction with one of two prototype drag-reducing surfaces: a regularly patterned "canonical" surface composed of periodic streamwise microgrooves, as well as a biomimetic random texture that can be fabricated using easily scalable surface treatment processes. The frictional drag reduction characteristics of these polymer-surface pairs were evaluated experimentally using a bespoke Taylor-Couette apparatus operating in the fully turbulent flow regime, at Reynolds numbers $15\,000 \leqslant \mathrm{Re}_s \leqslant 52\,000$.

Our results clearly indicate that considerable enhancements in the overall drag reduction in large Reynolds number flows can be achieved by combining a scalably textured superhydrophobic wall with dissolved polymer additives at suitable concentrations in the turbulent liquid phase. For example, at $\mathrm{Re}_s = 50\,000$, dissolved PAM at a concentration of 50 ppm yields a polymer-mediated drag reduction of approximately 18% [see Fig. 5(b)], whereas the randomly textured superhydrophobic wall by itself generates a comparable slip-induced drag reduction of about 17%. By combining the two techniques, an overall drag reduction of 27% can be achieved, which represents a 50% increase over the stand-alone drag reduction levels attainable from either method employed independently. Furthermore, we also anticipate that a concurrent deployment of polymer additives and superhydrophobic walls in this fashion will result in a "fail-safe" drag reduction strategy, capable of resilient operation over a wide range of Reynolds numbers and flow conditions: for example, at low Reynolds numbers, the superhydrophobic wall would provide continued friction reduction even in the laminar and transitional flow regimes where polymeric drag reduction is inoperative or ineffective, and at high Reynolds numbers the dissolved polymer chains would sustain a residual level of turbulent drag reduction even if the trapped air layer over the superhydrophobic wall is progressively lost due to fluctuation-induced plastron collapse [20].

Finally, we have also demonstrated that the physical adsorption of PEO chains at the air-water interface adversely influences the slip properties of the superhydrophobic random texture, and significantly diminishes the net reduction in frictional drag obtained. This strong surfactant effect may, in fact, partly serve to rationalize the surprising lack of prior reports on combined drag reduction in the literature, given the widespread use of PEO as a model polymer additive in experimental drag reduction investigations. The decisive role of interfacial effects, in turn, suggests that a careful evaluation of the surfactant activity of candidate drag-reducing polymers is a vital prerequisite for ensuring the successful design and implementation of combined drag reduction strategies in potential large-scale applications.

ACKNOWLEDGMENTS

The authors thank T. Van Buren and A. J. Smits at Princeton University for providing the grooved rotor used in this paper. Financial support for this work was provided in part by the Materials Research Science and Engineering Centers program of the National Science Foundation under Grant No. DMR-1419807, and by the the Office of Naval Research under the Multidisciplinary University Research Initiatives program through Contract No. 3002453814.

---

[1] H. Tennekes and J. L. Lumley, *A First Course in Turbulence* (MIT, Cambridge, MA, 1972).

[2] S. B. Pope, *Turbulent Flows* (Cambridge University, Cambridge, England, 2000).

[3] M. Perlin and S. Ceccio, *Mitigation of Hydrodynamic Resistance* (World Scientific, Singapore, 2015).

[4] S. A. Mäkiharju, M. Perlin, and S. L. Ceccio, On the energy economics of air lubrication drag reduction, Int. J. Nav. Arch. Ocean **4**, 412 (2012).

[5] J. W. Hoyt, The effect of additives on fluid friction, J. Basic Eng. **94**, 258 (1972).

[6] P. S. Virk, Drag reduction fundamentals, AIChE J. **21**, 625 (1975).

[7] N. S. Berman, Drag reduction by polymers, Annu. Rev. Fluid Mech. **10**, 47 (1978).

[8] C. M. White and M. G. Mungal, Mechanics and prediction of turbulent drag reduction with polymer additives, Annu. Rev. Fluid Mech. **40**, 235 (2008).

[9] M. D. Graham, Drag reduction and the dynamics of turbulence in simple and complex fluids, Phys. Fluids **26**, 101301 (2014).

[10] L. Xi, Turbulent drag reduction by polymer additives: Fundamentals and recent advances, Phys. Fluids **31**, 121302 (2019).

[11] W. J. Han, Y. Z. Dong, and H. J. Choi, Applications of water-soluble polymers in turbulent drag reduction, Processes **5**, 24 (2017).

[12] W. J. Han and H. J. Choi, Role of bio-based polymers on improving turbulent flow characteristics: materials and applications, Polymers **9**, 209 (2017).

[13] G. McHale, M. I. Newton, and N. J. Shirtcliffe, Immersed superhydrophobic surfaces: Gas exchange, slip and drag reduction properties, Soft Matter **6**, 714 (2010).

[14] J. P. Rothstein, Slip on superhydrophobic surfaces, Annu. Rev. Fluid Mech. **42**, 89 (2010).

[15] B. Bhushan and Y. C. Jung, Natural and biomimetic artificial surfaces for superhydrophobicity, self-cleaning, low adhesion, and drag reduction, Prog. Mater. Sci. **56**, 1 (2011).

[16] C. Lee, C.-H. Choi, and C.-J. Kim, Superhydrophobic drag reduction in laminar flows: A critical review, Exp. Fluids **57**, 176 (2016).

[17] K. B. Golovin, J. W. Gose, M. Perlin, S. L. Ceccio, and A. Tuteja, Bioinspired surfaces for turbulent drag reduction, Phil. Trans. R. Soc. A **374**, 20160189 (2016).

[18] S. Srinivasan, J. A. Kleingartner, J. B. Gilbert, R. E. Cohen, A. J. B. Milne, and G. H. McKinley, Sustainable Drag Reduction in Turbulent Taylor-Couette Flows by Depositing Scalable Superhydrophobic Surfaces, Phys. Rev. Lett. **114**, 014501 (2015).

[19] F. Schellenberger, N. Encinas, D. Vollmer, and H.-J. Butt, How Water Advances on Superhydrophobic Surfaces, Phys. Rev. Lett. **116**, 096101 (2016).

[20] K. Watanabe and H. Udagawa, Drag reduction of non-Newtonian fluids in a circular pipe with a highly water-repellent wall, AIChE J. **47**, 256 (2001).

[21] J. Seo, R. García-Mayoral, and A. Mani, Pressure fluctuations and interfacial robustness in turbulent flows over superhydrophobic surfaces, J. Fluid Mech. **783**, 448 (2015).

[22] H. Park, G. Sun, and C.-J. Kim, Superhydrophobic turbulent drag reduction as a function of surface grating parameters, J. Fluid Mech. **747**, 722 (2014).

[23] A. Rajappan, K. Golovin, B. Tobelmann, V. Pillutla, Abhijeet, W. Choi, A. Tuteja, and G. H. McKinley, Influence of textural statistics on drag reduction by scalable, randomly rough superhydrophobic surfaces in turbulent flow, Phys. Fluids **31**, 042107 (2019).

[24] A. Rajappan and G. H. McKinley, Polymers and plastrons in parallel yield enhanced turbulent drag reduction, Fluids **5**, 197 (2020).

[25] A. Rajappan and G. H. McKinley, Epidermal biopolysaccharides from plant seeds enable biodegradable turbulent drag reduction, Sci. Rep. **9**, 18263 (2019).

[26] C. D. Andereck, S. S. Liu, and H. L. Swinney, Flow regimes in a circular Couette system with independently rotating cylinders, J. Fluid Mech. **164**, 155 (1986).

[27] G. S. Lewis and H. L. Swinney, Velocity structure functions, scaling and transitions in high Reynolds number Couette-Taylor flow, Phys. Rev. E **59**, 5457 (1999).

[28] R. Pamies, J. G. H. Cifre, M. del Carmen López Martínez, and J. G. de la Torre, Determination of intrinsic viscosities of macromolecules and nanoparticles. comparison of single-point and dilution procedures, Colloid Polym. Sci. **286**, 1223 (2008).

[29] M. Rubinstein and R. H. Colby, *Polymer Physics* (Oxford University, New York, 2003).

[30] K. J. McCarthy, C. W. Burkhardt, and D. P. Parazak, Mark-Houwink-Sakurada constants and dilute solution behavior of heterodisperse poly(acrylamide-co-sodium acrylate) in 0.5 M and 1 M NaCl, J. Appl. Polym. Sci. **33**, 1699 (1987).

[31] F. E. Bailey, J. L. Kucera, and L. G. Imhof, Molecular weight relations of poly(ethylene oxide), J. Polym. Sci. **32**, 517 (1958).

[32] R. L. Panton, Scaling laws for the angular momentum of a completely turbulent Couette flow, C. R. Acad. Sci. Ser. B **315**, 1467 (1992).

[33] J. R. Philip, Flows satisfying mixed no-slip and no-shear conditions, Z. Angew. Math. Phys. **23**, 353 (1972).

[34] T. Min and J. Kim, Effects of hydrophobic surface on skin-friction drag, Phys. Fluids **16**, L55 (2004).

[35] C. T. Fairhall and R. García-Mayoral, Spectral analysis of the slip-length model for turbulence over textured superhydrophobic surfaces, Flow Turbul. Combust. **100**, 961 (2018).

[36] T. R. Scavo and J. B. Thoo, On the geometry of Halley's method, Am. Math. Mon. **102**, 417 (1995).

[37] M. W. Kim and B. H. Cao, Additional reduction of surface tension of aqueous polyethylene oxide (PEO) solution at high polymer concentration, Europhys. Lett. **24**, 229 (1993).

[38] C.-E. Brunchi, M. Bercea, S. Morariu, and M. Dascalu, Some properties of xanthan gum in aqueous solutions: Effect of temperature and pH, J. Polym. Res. **23**, 123 (2016).

[39] F. J. Peaudecerf, J. R. Landel, R. E. Goldstein, and P. Luzzatto-Fegiz, Traces of surfactants can severely limit the drag reduction of superhydrophobic surfaces, Proc. Natl. Acad. Sci. USA **114**, 7254 (2017).

[40] R. Y. Z. Hu, A. T. A. Wang, and J. P. Hartnett, Surface tension measurement of aqueous polymer solutions, Exp. Therm. Fluid Sci. **4**, 723 (1991).

[41] Y. F. Yano, Correlation between surface and bulk structures of alcohol-water mixtures, J. Colloid Interface Sci. **284**, 255 (2005).

[42] K. Alamé, S. Anantharamu, and K. Mahesh, A variational level set methodology without reinitialization for the prediction of equilibrium interfaces over arbitrary solid surfaces, J. Comput. Phys. **406**, 109184 (2020).